A Novel Low-Dose Dual-Energy Imaging Method for a Fast-Rotating Gantry-Type CT Scanner

Sanghoon Cho, Seoyoung Lee, Jongha Lee, Donghyeon Lee, Hyoyi Kim, Jong-Hyun Ryu, Kilhwan Jeong, Kyu-Gyum Kim, Kwon-Ha Yoon, and Seungryong Cho, *Senior Member, IEEE*

***Abstract*— CT scan by use of a beam-filter placed between the x-ray source and the patient allows a single-scan low-dose dual-energy imaging with a minimal hardware modification to the existing CT systems. We have earlier demonstrated the feasibility of such imaging method with a multi-slit beam-filter reciprocating along the direction perpendicular to the CT rotation axis in a cone-beam CT system. However, such method would face mechanical challenges when the beam-filter is supposed to cooperate with a fast-rotating gantry in a diagnostic CT system. In this work, we propose a new scanning method and associated image reconstruction algorithm that can overcome these challenges. We propose to slide a beam-filter that has multi-slit structure with its slits being at a slanted angle with the CT gantry rotation axis during a scan. A streaky pattern would show up in the sinogram domain as a result. Using a notch filter in the Fourier domain of the sinogram, we removed the streaks and reconstructed an image by use of the filtered-backprojection algorithm. The remaining image artifacts were suppressed by applying l_0 norm based smoothing. Using this image as a prior, we have reconstructed low- and high-energy CT images in the iterative reconstruction framework. An image-based material decomposition then followed. We conducted a simulation study to test its feasibility using the XCAT phantom and also an experimental study using the Catphan phantom, a head phantom, an iodine-solution phantom, and a monkey in anesthesia, and showed its successful performance in image reconstruction and in material decomposition.**

Manuscript received November 11, 2020; accepted December 9, 2020. Date of publication December 14, 2020; date of current version March 2, 2021. This work was supported in part by the Korean National Research Foundation under Grant 2016M3A9E9941837, Grant 2018M3A9E9024949, Grant 2019M2A2A4A05031487, and Grant 2020R1A2C2011959; in part by the KUSTAR-KAIST Institute, KAIST, Korea; and in part by the institute of Civil Military Technology Cooperation funded by the Defense Acquisition Program Administration and Ministry of Trade, Industry and Energy of Korean government under Grant UM19207RD2. *(Corresponding author: Seungryong Cho.)*

Sanghoon Cho, Seoyoung Lee, Jongha Lee, Donghyeon Lee, and Hyoyi Kim are with the Department of Nuclear and Quantum Engineering, KAIST, Daejeon 34141, South Korea.

Jong-Hyun Ryu, Kilhwan Jeong, and Kyu-Gyum Kim are with the Medical Convergence Research Center, Wonkwang University, Iksan 570-749, South Korea.

Kwon-Ha Yoon is with the Medical Convergence Research Center, Wonkwang University, Iksan 570-749, South Korea, and also with the Department of Radiology, School of Medicine, Wonkwang University, Iksan 570-749, South Korea.

Seungryong Cho is with the Department of Nuclear and Quantum Engineering, KAIST, Daejeon 34141, South Korea, and also with the KAIST Institutes for ICT, HST, and AI, KAIST, Daejeon 34141, South Korea (e-mail: scho@kaist.ac.kr).

Digital Object Identifier 10.1109/TMI.2020.3044357

***Index Terms*— Low-dose CT, dual-energy CT, CT image Reconstruction.**

I. Introduction

RICH image information in x-ray computed tomography (CT) comes at nonzero cost of radiation dose to the patient. To reduce health risks, there have been active researches on low-dose imaging without sacrificing diagnostic image information. One straightforward method is to lower x-ray tube current with appropriate denoising processes embedded before/during/after image reconstruction. Most commercial diagnostic CT systems indeed use a few iterations between the data domain and the image domain for denoising after an initial filtered-backprojection (FBP) image reconstruction [1], [2]. Advanced fully iterative algorithms are also in use that exploit the x-ray source and detector characteristics and prior information of the assumed noise model [3]–[7]. Off the reconstruction engine, data domain denoising or sinogram restoration approaches have been actively studied [8]–[11]. Reconstructed image domain denoising techniques have also been developed including total variation minimization filtering [12], [13], nonlocal means (NLM) filtering [14]–[16], k-singular vector decomposition (SVD) [17], and patch-based denoising schemes [18], [19].

Another viable option to low-dose CT imaging is sparse sampling approach. Although it has not been adopted in a commercialized diagnostic CT system, perhaps mostly due to the hardware challenge related to fast and stable power switching, sparse-view sampling that reduces the total number of projections has been actively investigated particularly in the context of image reconstruction [20]–[23]. It may be of particular interest in flat-panel based cone-beam CT (CBCT) imaging systems where gantry rotation speed is lower by almost two orders of magnitude than that of diagnostic CT systems. Indeed, there exist a host of articles that report sparse-view image reconstruction in CBCT settings despite the real implementation of on-off power switching is not necessarily enforced yet [24], [25]. As an alternative to the sparse-view sampling, we have earlier proposed a many-view under-sampling (MVUS) technique that uses a multi-slit beam-blocker [26]–[28]. By use of a reciprocating multi-slit radio-opaque blocker placed between the x-ray source and the patient, radiation dose can be substantially reduced. Compressed-sensing inspired iterative image reconstruction

algorithm can reconstruct images from such sparsely sampled data [26]. We demonstrated its experimental feasibility in a benchtop CBCT system [27], [28].

Dual-energy imaging and its associated material decomposition capability are highly desirable for accurate diagnosis particularly when the CT number of contrast agent is similar to that of lesion (e.g., calcium plaque in the blood vessel). High-end CT systems are usually equipped with the dual-energy scanning option. They employ various methods for dual-energy scan such as fast kV-switching [29], [30], dual-source technology [31], [32], dual-layer detector [33], energy-discriminating detector [34]–[37], primary modulation method [38], and use of spectral CT filters [39], [40]. Our proposed method, as will be detailed later, not only offers an alternative way of dual-energy scan but also enables it at an inherently low-dose manner. Another attractive point is that the proposed technique can be applied to the existing low-end CT systems too with a minimal hardware addition, although cooperation with the commercial CT vendors is needed for accessing raw-data.

We have shown earlier in a CBCT setting that a low-dose single-scan dual-energy imaging for material decomposition is possible in the MVUS framework by replacing multi-slit beam-blocker by multi-slit beam-filter [28]. X-ray beam through the slits forms low-energy projection data while the beam passing through the filter material forms relatively high-energy projection data. Despite of its successful implementation in a CBCT setting where a multi-slit beam-filter reciprocating along the direction perpendicular to the CT rotation axis, such reciprocation motion would be mechanically challenging in a fast-rotating gantry based diagnostic CT system. Increased penumbra effects of the beam-filter edges would also add an additional burden. Note that the beam-filter should be placed within the gantry housing of a diagnostic CT system, which may lead to a larger geometric magnification of the beam-filter projections compared to the housing-free CBCT. Due to the penumbra, substantial portions of the data would be subject to waste.

In this work, we propose a new beam-filter based scanning method and associated image reconstruction algorithm for a diagnostic CT system that can overcome these challenges. Instead of using a reciprocating motion of the beam-filter, we propose to use a linear motion of a beam-filter that has multi-slit structure with the slits being at a slanted angle with the CT gantry rotation axis. The proposed approach can solve the aforementioned mechanical challenge. In addition, penumbra regions caused by beam-filter edges can be fully used for prior image reconstruction as will be detailed in the following section in this study, whereas our earlier method can use only penumbra-free regions for image reconstruction. Both simulation and experimental studies to validate the proposed method have been conducted.

II. Materials and Methods

A. MVUS Scheme With a Slanted Multi-Slit Beam-Filter

The proposed MVUS scheme for low-dose CT imaging that utilizes a multi-slit beam-filter is shown in Fig. 1, where the

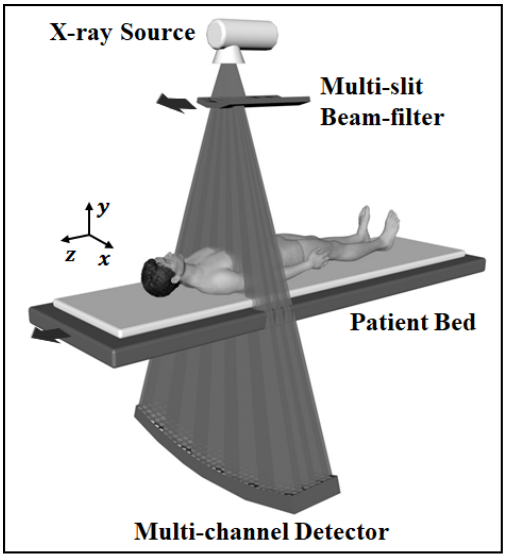

Fig. 1. Schematic of the proposed scanning configuration. The arrows indicate the motion of the beam-filter and that of the patient couch.

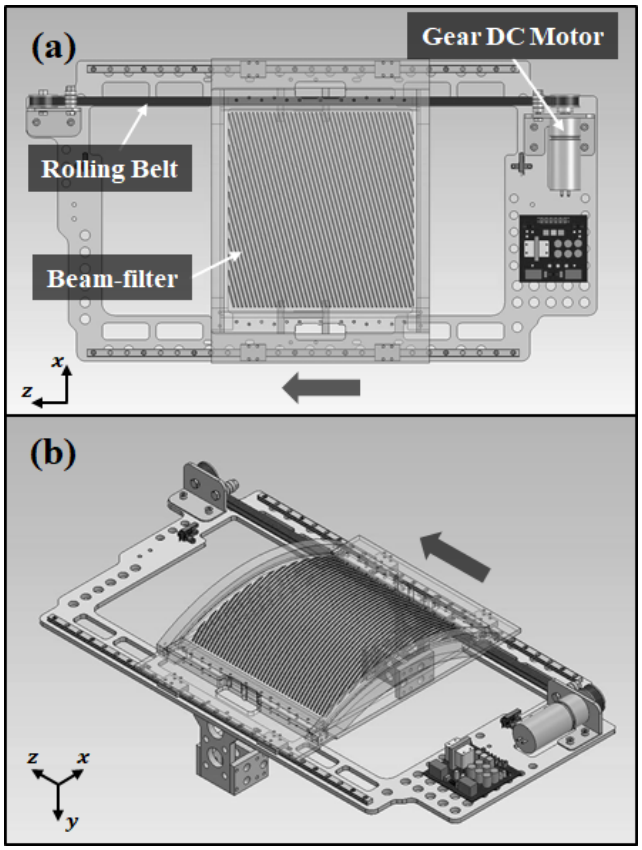

Fig. 2. (a) Front-view and (b) birds' eye view of the designed beam-filter.

beam-filter partially attenuates x-ray photons leading to a lower exposure to the patient. The beam-filter is mounted on a rolling belt with a DC gear motor and linearly moves along with the patient bed at a constant speed as shown in Fig. 2 (a). The material and thickness of the beam-filter can be chosen for effective beam-energy shifting and also for reducing radiation dose; in this work, 1 mm-thick Sn filter was used for

the experimental study. The multi-slit structured filtering-strips are aligned on a curved acrylic plate at a slanted angle so that the x-ray beam is also split into high- and low-energy beams in a slanted form leading to a streaky sinogram. Since the mean energy of the spectrum of x-ray passing through the filtering strips shifts to a higher level, the unfiltered- and filtered- signals would form low- and high-energy projection, respectively. The beam-filter surface is curved so as to take care of the beam-divergence and minimizing the penumbra of the beam-filter strip edges in this work. Since the focal spot size of the x-ray is finite, the penumbra would occur even in this curved beam-filter. However, the effects of such penumbra would be even aggravated in the flat-panel-detector case as the magnification factor increases across the FOV. Because the diagnostic gantry-based CT usually has a curved array of detector elements unlike the flat-panel-detector in the conventional CBCT systems, penumbra effects should be accordingly reduced with such a curved surface of the beam-filter. Without loss of generality, in this work only a circular fan-beam scan is considered. Extending the method to a helical scan would be straightforward as will be briefly discussed later in this paper.

In our earlier implementation of MVUS in the CBCT setting, reciprocation of the multi-slit perpendicular to the rotation axis was found to yield optimum image quality at its frequency of 30 cycles/2π-rotation [27], [28]. Therefore, realization of such moving filter in a fast-rotating gantry, typically up to 1 - 4 rotations per second, is not feasible due to mechanical stability issues. On the other hand, the proposed beam-filter moving in one way along z-direction at a reasonably slow speed, as shown in Fig. 1, provides an available hardware implementation of beam-filter in the fast gantry-rotation. Such a linear motion of the slanted multi-slit beam-filter turns out to allow a fairly uniform data sparse sampling across the entire field-of-view (FOV) as well. In addition, the total stroke of the beam-filter motion is constrained by the size of space within the gantry housing, which is found to be sufficient in this work scope.

B. Image Reconstruction and Dual-Energy Imaging Algorithms

As shown in Fig.3, overall image reconstruction algorithm developed in this work consists of 2 steps: (1) Initial image reconstruction step for acquiring structural information of the image, and (2) dual-energy image reconstruction via prior-image based iterative algorithm followed by image-domain material decomposition. Detailed description of the methodology is presented in the following.

C. Step1: Initial Image Reconstruction

Figure 4 shows a schematic workflow in the initial image reconstruction. Out of the streaky sinogram acquired by the proposed scanning method, we want to come up with a CT image of which anatomical structure information is intact. Even though local CT numbers are off the ground-truth, it should be okay since those CT numbers can be accurately recovered in the second reconstruction engine for dual-energy

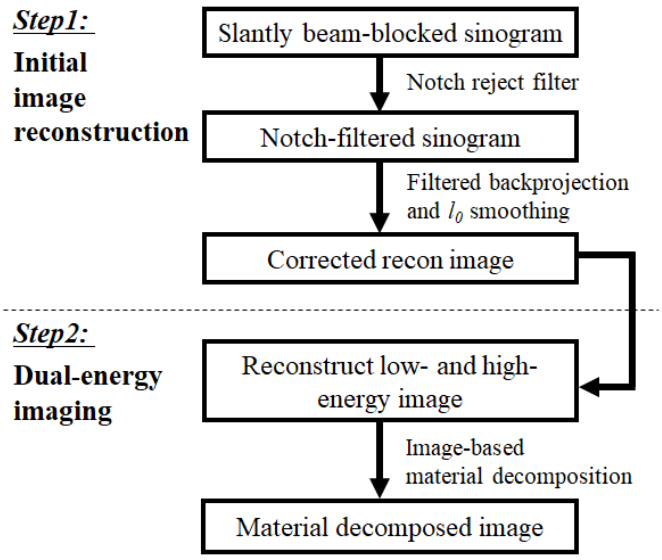

Fig. 3. Flowchart of the proposed method.

imaging. The point is that the sound information of the anatomical structures in the initially reconstructed image can translate to and facilitate of the following dual-energy image reconstruction. To achieve such an initial image reconstruction, we have devised a novel pre- and post-reconstruction image processing chain.

Input sinogram, shown in the left bottom of Fig. 4, is of oblique streaks corresponding to the moving beam-filter as explained before. Note that the Fourier transform of the streaks in a repetitive pattern in the image would result in pairs of impulses located at the conjugate frequencies. After applying Canny edge detection to the sinogram, we designed a Gaussian notch filter to remove corresponding streaks in the image. Optimal notch filter was determined by minimizing local variance of the restored estimate. The Gaussian notch reject filter is expressed by

$$\vec{H}_{NR}(u,v) = \prod_{k=1}^{Q} \vec{H}_k(u,v)\,\vec{H}_{-k}(u,v), \tag{1}$$

where $\vec{H}_k(u,v)$ and $\vec{H}_{-k}(u,v)$ are Gaussian highpass filteres whose centers are at (u_k, v_k) and (u_{-k}, v_{-k}), respectively, and Q is the total number of pairs of impulses. Note that double-wedge region in the Fourier transformed domain of a sinogram contains most of the structural information, which is also known as frequency-distance principle [41], [42] and that the slope of the sequence of conjugate impulses depends on the slope of the streaks in the sinogram. As shown in the Fourier transform of the streaky sinogram in Fig. 4, double-wedge part can be well separated from the conjugate impulses by appropriately adjusting the slope of the streaks. Please note that a static beam-filter would lead to a horizontal sequence of impulses substantially interfering with the structural information part and that the notch-filtering process in such case can lead to a heavy structural information loss.

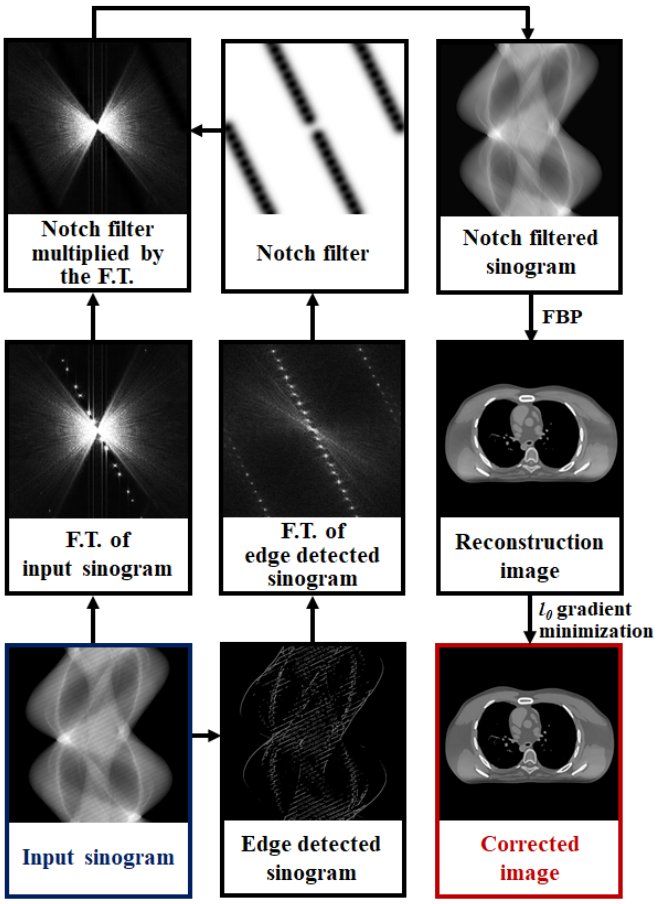

Fig. 4. Flowchart of the pre- and post-reconstruction image processing for an initial image reconstruction.

Subsequently, the streak-free sinogram is fed into the conventional FBP algorithm for image reconstruction. In case when undesirable residual image artifacts arise from an incomplete streak removal, we apply l_0 gradient minimization of image gradient, which is known to be an effective denoiser [43]. Corrected sinogram $\vec{g}^{cor}$ and corrected reconstruction image $\vec{f}^{cor}$ are mathematically represented by:

$$\vec{g}^{cor} = \mathcal{F}^{-1}\left[\vec{H}_{NR}(u,v)\cdot\vec{G}(u,v)\right] \tag{2}$$

$$\vec{f}^{cor} = \left(\left(\vec{f} - \mathrm{R}^{-1}\left\{\vec{g}^{cor}\right\}\right)^2 + \lambda\cdot\left\|\nabla\vec{f}\right\|_0\right) \tag{3}$$

where $\vec{G}$ is the Fourier transform of the measured data $\vec{g}$, R^{-1} represents the FBP operator, and λ is a weight that controls the amount of smoothing.

Partly due to this pre- and post- reconstruction image processing, the reconstructed voxel values do not present real attenuation information of the object either at high or low x-ray energy. However, we can utilize the anatomical structural information as a prior for further iterative image reconstruction in the compressed sensing inspired framework, which will be explained in the following subsection. One of the key novelties of the proposed technique lies in the fact that one can fully utilize the sinogram data even with the streaks related to the beam-filtration.

D. Step2: Dual-Energy Image Reconstruction and Material Decomposition

With an appropriate masking process, low- and high- energy projection data can be separately prepared and then can be fed into the dual-energy image reconstruction. In this step, we discard the data corresponding to the penumbra. A constrained total-variation minimization algorithm was implemented for such image reconstruction [20]–[23]. The mask used in the masking process can be obtained with the help of the notch filter used in the sinogram restoration process. Based on the multi-slit edge images outlined by the notch filter, we have added margins to exclude penumbra regions so that pure low- and high-energy projection data can be selected. The size of margins have been empirically determined.

The image reconstruction algorithm minimizes l_2 norm of the difference between gradient magnitude image (GMI) of the prior image and the image to be reconstructed together with the total-variation of the image under the constraint of data fidelity. Let $\vec{f}^{cor}$ denote the prior corrected image obtained in the initial image reconstruction. GMI is represented by:

$$GMI_{i,j,k} = \sqrt{\left|\begin{array}{l}\left(f_{i,j,k} - f_{i-1,j,k}\right)^2 + \left(f_{i,j,k} - f_{i,j-1,k}\right)^2 \\ + \left(f_{i,j,k} - f_{i,j,k-1}\right)^2\end{array}\right|}, \tag{4}$$

where i, j, and k are voxel indices. The l_2 norm of difference between GMI of the prior image and the image is presented as following:

$$\left\|GMI^{cor} - GMI\right\|_2 = \sqrt{\sum\left(\begin{array}{l}\sqrt{\left(f^{cor}_{i,j,k} - f^{cor}_{i-1,j,k}\right)^2 + \left(f^{cor}_{i,j,k} - f^{cor}_{i,j-1,k}\right)^2} \\ \quad + \left(f^{cor}_{i,j,k} - f^{cor}_{i,j,k-1}\right)^2 \\ - \sqrt{\left(f_{i,j,k} - f_{i-1,j,k}\right)^2 + \left(f_{i,j,k} - f_{i,j-1,k}\right)^2} \\ \quad + \left(f_{i,j,k} - f_{i,j,k-1}\right)^2\end{array}\right)^2} \tag{5}$$

Both low- and high-energy CT image reconstructions leverage the joint sparsity with the prior in this way. We used a gradient descent optimization method for GMI minimization in which partial derivative of Eq. (6) with respect to each voxel value are calculated. Low-energy image $\vec{f}^{low}$ and high-energy image $\vec{f}^{high}$ are then obtained by solving minimization problems of Eqs. (7) and (8), respectively:

$$\vec{f}^{low} = \arg\min_{f^*}\left(\left\|\vec{f}^{low}\right\|_{TV} + \beta\left\|GMI^{cor} - w_1 GMI^{low}\right\|_2\right)$$
$$\text{such that } \left\|A\vec{f}^{low} - \vec{g}^{low}\right\| < \varepsilon_1 \text{ and } \vec{f}^{low} \geq 0 \tag{6}$$

$$\vec{f}^{high} = \arg\min_{f^*}\left(\left\|\vec{f}^{high}\right\|_{TV} + \beta\left\|GMI^{cor} - w_2 GMI^{high}\right\|_2\right)$$
$$\text{such that } \left\|A\vec{f}^{high} - \vec{g}^{high}\right\| < \varepsilon_2 \text{ and } \vec{f}^{high} \geq 0 \tag{7}$$

where $\vec{g}^{low}$ and $\vec{g}^{high}$ correspond to the low- and high-energy projection data selected after the masking process. w_1 and w_2 correspond to the ratio of l_1 norm of GMI^{cor} to that of GMI^{low} and the ratio of l_1 norm of GMI^{cor} to that of GMI^{high}, respectively, and they are purposely incorporated for normalizing different GMI scales between them [44]. Pseudo-code of the algorithm is summarized in table I, and the balance among POCS update, TV minimization update, and GMI minimization update and detailed optimization process with parameters α_{POCS}, α_{TV}, α_{GMI}, n_{TV}, n_{GMI}, and stopping criteria for main iteration are largely borrowed from the references with their empirical tuning to our system [22], [28].

After the dual-energy image reconstruction, the images are fed into an image-based material decomposition algorithm. Through an empirical calibration process, we present mean CT numbers of basis materials: soft-tissue images by $\bar{\vec{f}}^{low}_{tissue}$ and $\bar{\vec{f}}^{high}_{tissue}$, bone images by $\bar{\vec{f}}^{low}_{bone}$ and $\bar{\vec{f}}^{high}_{bone}$, and air images by $\bar{\vec{f}}^{low}_{air}$, and $\bar{\vec{f}}^{high}_{air}$. A calibration process constructs a matrix relationship between the dual-energy CT numbers and the volume fraction of each tissue type. Finally, material decomposition is performed by calculating volume fractions $\vec{V}$ of each material by solving the inverse linear algebra [45]:

$$\begin{bmatrix} \vec{V}_{tissue} \\ \vec{V}_{bone} \\ \vec{V}_{air} \end{bmatrix} = \begin{bmatrix} \bar{\vec{f}}^{low}_{tissue} & \bar{\vec{f}}^{low}_{bone} & \bar{\vec{f}}^{low}_{air} \\ \bar{\vec{f}}^{high}_{tissue} & \bar{\vec{f}}^{high}_{bone} & \bar{\vec{f}}^{high}_{air} \\ 1 & 1 & 1 \end{bmatrix}^{-1} \begin{bmatrix} \vec{f}^{low} \\ \vec{f}^{high} \\ 1 \end{bmatrix} \quad (8)$$

E. Simulation Study

Simulation study was conducted using the 3D digital anthropomorphic XCAT phantom [46]. The forward projection model took into account the x-ray energy spectrum so that mean energy difference between the unfiltered (120 kVp) and the filtered (120 kVp with Sn filter of 1 mm thickness) regions, 50% of total area each, can be incorporated. 0.1% Gaussian noise, and 0.07% and 0.37% Poisson noise were added to the unfiltered and to the filtered region, respectively, following the modeling procedures described in the reference [47]. Penumbra effect was also considered by smoothly connecting the non-filtered and filtered regions in a polynomial form. The number of filter strips was set to be 6 with 3 cycles/rotation in a sinogram, of which the detailed optimization process is summarized in Appendix. In this work, a fan-beam circular scanning geometry was used to test the feasibility of the proposed method. Two input sinograms of lung and abdomen parts are shown in Fig. 5.

F. Experimental Study

Experiments were conducted on a prototype diagnostic CT system we built at Wonkwang University School of Medicine, of which raw data can be accessed [48]. Figure 6 (a) shows the pictures of the system with the manufactured beam-filter mounted in front of the x-ray beam outlet. Table II summarizes the system configurations. The gantry rotation speed was

TABLE I
PSEUDO-CODE IMPLEMENTATION OF POCS-TV RECONSTRUCTION ALGORITHM UTILIZING GMI REGULARIZER

$\alpha_{POCS} \coloneqq 0.94; \alpha_{POCS,red} \coloneqq 0.97;$
$\alpha_{TV} = 0.2;\ \alpha_{TV,red} = 0.94;$
$\alpha_{GMI} = 0.1;\ \alpha_{GMI,red} = 0.97;$
$n_{TV} \coloneqq 5; n_{GMI} \coloneqq 5; r = 0.95;$
$\vec{f} \coloneqq \vec{f}^{cor}$
repeat $\{iteration\}$
  $\vec{f_0} \coloneqq \vec{f}$
  for $j = 1, N_d$ **do** $\{POCS\ update\}$
    $\vec{f} \coloneqq \vec{f} + \alpha_{POCS}\vec{H}_j \dfrac{\vec{g}_j - \vec{H}_j \cdot \vec{f}}{\vec{H}_j \cdot \vec{H}_j}$
  end for
  for $k = 1, N_k$ **do** $\{Positivisy\ update\}$
    if $f_k < 0$ **then**
      $f_k = 0$
    end if
  end for
  $\tilde{g} \coloneqq H\vec{f}$
  $dd \coloneqq |\tilde{g} - \vec{g}|$
  $ad \coloneqq |\vec{f} - \vec{f_0}|$
  if {first iteration} **then**
    $\alpha_{TV} \coloneqq \alpha_{TV} \times ad, \alpha_{GMI} \coloneqq \alpha_{GMI} \times ad$
  end if
  $\vec{f_0} \coloneqq \vec{f}$
  for $j = 1, n_{TV}$ **do** $\{TV\ minimization\ update\}$
    $d\vec{f}_{TV} \coloneqq \nabla_{\vec{f}} \|\vec{f}\|_{TV}$
    $\vec{f} \coloneqq \vec{f} - \alpha_{TV} * \dfrac{d\vec{f}_{TV}}{|d\vec{f}_{TV}|}$
  end for
  $gd \coloneqq |\vec{f} - \vec{f_0}|$
  if $gd > r \times ad$ **and** $dd > \epsilon$ **then**
    $\alpha_{TV} \coloneqq \alpha_{TV} \times \alpha_{TV,red}$
  end if
  for $j = 1, n_{GMI}$ **do** $\{GMI\ minimization\ update\}$
    $d\vec{f}_{GMI} \coloneqq \nabla_{\vec{f}} \|GMI^{cor} - wGMI\|_2$
    $\vec{f} \coloneqq \vec{f} - \alpha_{GMI} * \dfrac{d\vec{f}_{GMI}}{|d\vec{f}_{GMI}|}$
  end for

TABLE I
(Continued.) PSEUDO-CODE IMPLEMENTATION OF POCS-TV RECONSTRUCTION ALGORITHM UTILIZING GMI REGULARIZER

$gd \coloneqq \left|\vec{f} - \vec{f}_0\right|$
if $gd > r \times ad$ **and** $dd > \epsilon$ **then**
  $\alpha_{GMI} \coloneqq \alpha_{GMI} \times \alpha_{GMI,red}$
end if
$\alpha_{POCS} \coloneqq \alpha_{POCS} \times \alpha_{POCS,red}$
until stop
$\vec{f}^* = \vec{f}$
return $\vec{f}^*$

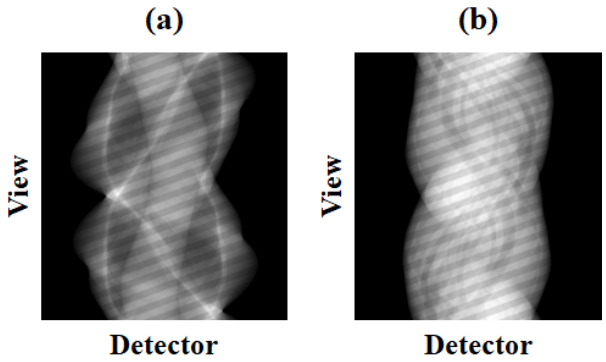

Fig. 5. Sinograms of (a) lung and (b) abdomen parts of anthropomorphic XCAT phantom.

TABLE II
SCANNING PARAMETERS

Parameters	Values
Views per rotation	1440
Gantry rotation speed	1 rotation / 1 sec
Detector pixel number	888 × 16
Detector pixel pitch	1.08mm × 1 mm
Distance of source to detector	1008 mm
Distance of source to object	534 mm
Field of view	500 mm
X-ray	120 kVp / 200 mA

set to be 1 turn per 1 second in this feasibility study. The multi-channel detector is composed of 888 × 16 pixels with 1.08 mm × 1 mm pixel pitch. 1440 views of projection were obtained in 1 rotation with no couch motion, and the x-ray was operated at the tube voltage of 120 kVp and the tube current of 250 mA. The beam-filter was linearly translated during a scan in the direction of the gantry rotation axis as shown by the arrow in Fig. 6 (b). The travel distance of the beam-filter in a single rotation of the gantry was about 80 mm. The beam-filter is composed of 92 Sn strips with each strip's thickness of 1 mm supported by a curved acrylic plate, and the ratio of the widths of unfiltered to the filtered area was set to be 1:1 in this work. The total width of the beam-filter plate is 241 mm and 221 mm along x- and z-axis, respectively.

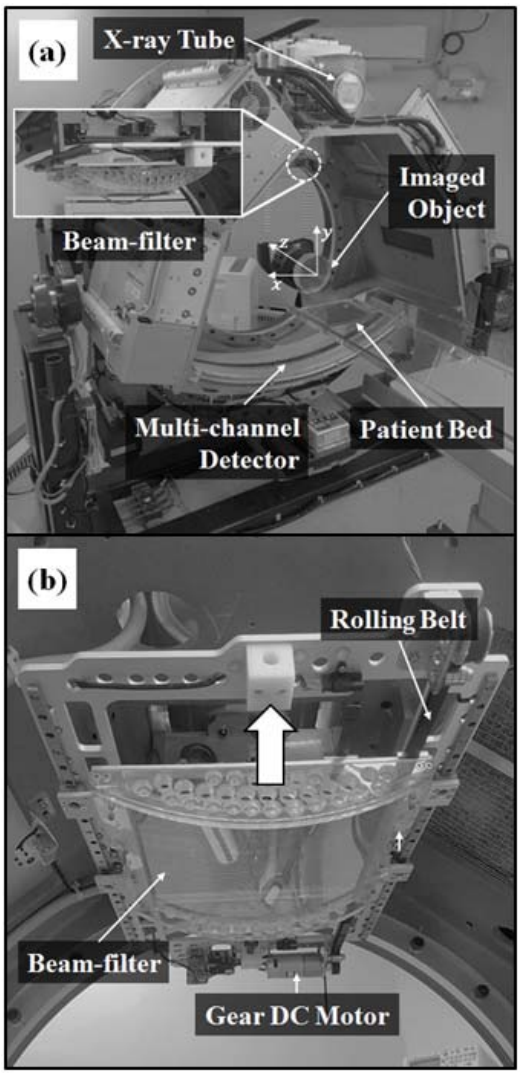

Fig. 6. (a) Prototype diagnostic CT system and (b) a mounted slanted-type beam-filter.

The homogeneous unit and the contrast unit of the Catphan phantom (Phantom Laboratory, NY, USA) were used for the scanned object [49]. Accordingly, quantitative evaluations of the degree of uniformity and contrast in the reconstructed images have been performed. In addition, the Angiographic CT Head Phantom ACS PH-3 (Kyoto Kagaku Co., Ltd, Kyoto, Japan) was scanned for demonstrating a more realistic situation. Iodine solution phantom was used for a quantitative evaluation of the material decomposition. We have also scanned a monkey in anesthesia. Figure 7 shows the spectral shift of the x-ray energy after beam filtration with 1mm thick Sn using the Spektr computational tools [50]. The mean energies of the unfiltered and the filtered x-ray were calculated to be 52.5 keV and 89.6 keV, respectively.

G. Image Quality Assessment

Structural similarity (SSIM) was evaluated by:

$$SSIM\,(x, y) = \frac{\left(2n_x n_y + c_1\right)\left(2\sigma_{xy} + c_2\right)}{\left(n_x^2 + n_y^2 + c_1\right)\left(\sigma_x^2 + \sigma_y^2 + c_2\right)} \tag{9}$$

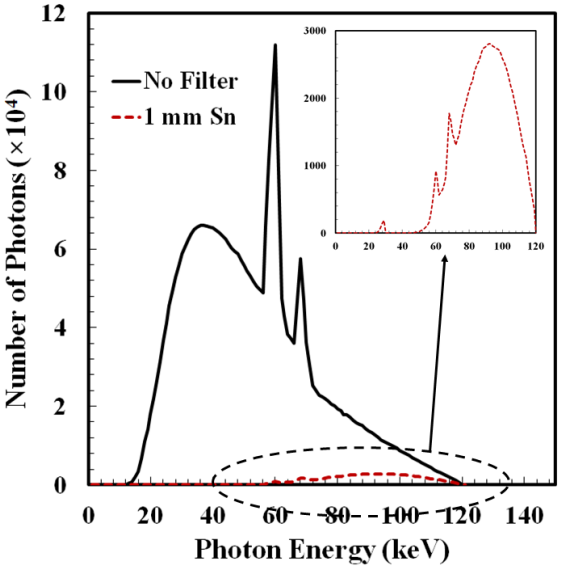

Fig. 7. The spectrum of the x-ray at 120kVp with and without Sn filter.

where n_x and n_y denote the mean values of images x and y, σ_x and σ_y are the standard deviation of x and y, respectively, and σ_{xy} is the covariance between x and y. c_1 and c_2 are small positive constants.

Image uniformity was calculated by using the following equation:

$$t_{cup}\,(\%) = 100 \times \frac{\overline{\mu}_{edge} - \overline{\mu}_{center}}{\overline{\mu}_{edge}} \tag{10}$$

where $t_{cup}\,(\%)$ is the magnitude of the cupping artifact, and $\overline{\mu}_{edge}$ and $\overline{\mu}_{center}$ are average values of the reconstructed image at the edge and at the center region, respectively, of the homogeneous unit of the Catphan phantom.

Contrast was evaluated by following equation:

$$contrast = \frac{|\bar{n}_1 - \bar{n}_2|}{\bar{n}_2} \tag{11}$$

where $\bar{n}_1$ and $\bar{n}_2$ are the mean values of the region-of-interest (ROI) and the background, respectively.

Contrast-to-noise ratio (CNR) was calculated as following:

$$CNR = \frac{|\bar{n}_1 - \bar{n}_2|}{\sqrt{\sigma_1^2 + \sigma_2^2}} \tag{12}$$

where σ_1 and σ_2 represent the standard deviations of each region.

III. Results

A. Simulation Results

Figures 8 and 9 show the image reconstruction results of lung and abdomen part of the XCAT phantom, respectively. In both figures, (a) shows the reconstructed image using fully unblocked sinogram at low-energy x-ray spectrum as a gold standard, (b) shows the reconstructed image by FBP without any processing from the streaky sinogram, (c) shows the reconstructed image by FBP with the streak-removal processing, and (d) presents the reconstructed image by FBP with the

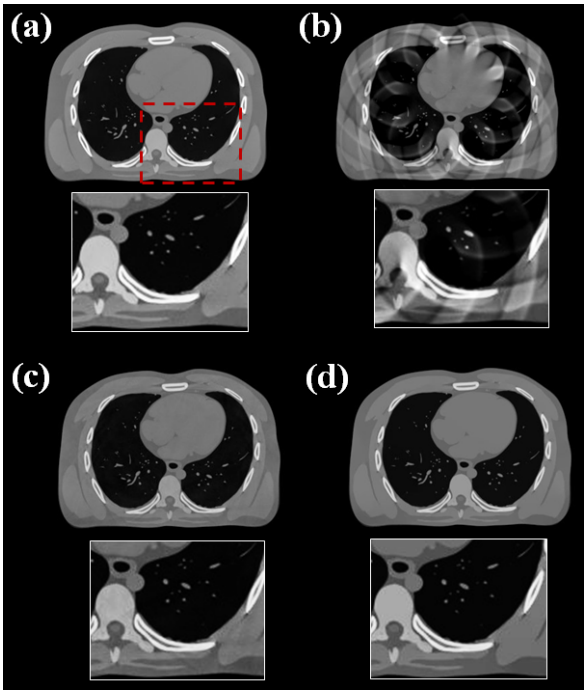

Fig. 8. (a) Reconstructed image using unblocked Sinogram as gold standard, (b) Image from the streaky Sinogram without any processing, (c) Image from the Processed Sinogram, and (d) Image from the processed Sinogram followed by l_0 gradient minimization of Lung XCAT phantom. The display window is [0.0036 mm^{-1}, 0.0383 mm^{-1}].

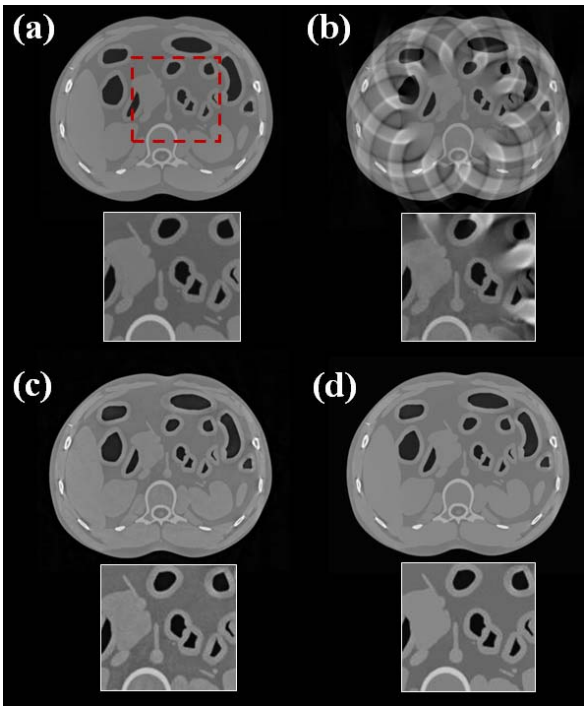

Fig. 9. (a) Reconstructed image using unblocked Sinogram as gold standard, (b) Image from the streaky Sinogram without any processing, (c) Image from the processed Sinogram, and (d) Image from the processed Sinogram followed by l_0 gradient minimization of abdomen XCAT phantom. The display window is [0.0000 mm^{-1}, 0.03612 mm^{-1}].

streak-removal process followed by l_0 gradient minimization in the image domain. As can be seen in the zoomed-in figures, partially beam-filtered streaky sinogram without any image

TABLE III
CALCULATED SSIM VALUES FOR THE CASES OF (b), (c), AND (d) IN FIG. 8 AND 9

SSIM	(b)	(c)	(d)
Lung	0.9882	0.9985	0.9990
Abdomen	0.9093	0.9607	0.9991

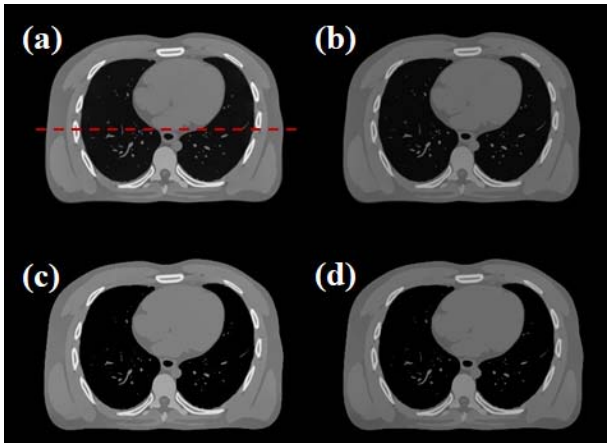

Fig. 10. (a) Low- and (b) high-energy ground truth images, and (c) low- and (d) high-energy reconstructed images using the proposed method of a lung XCAT phantom. The display window is [0.0033 mm^{-1}, 0.0402 mm^{-1}].

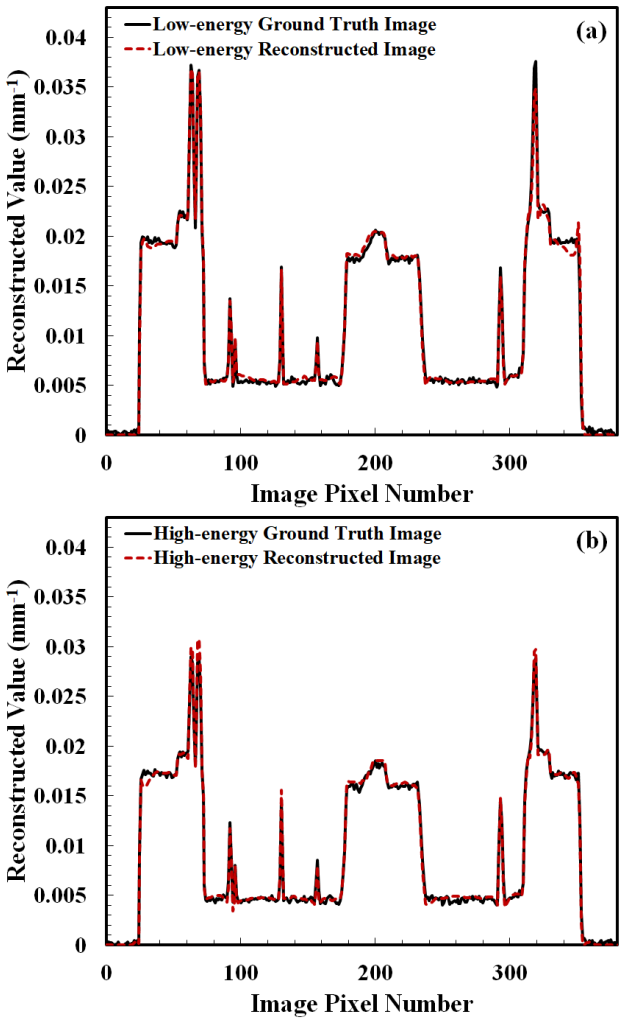

Fig. 11. (a) Line profiles of low-energy ground truth image and reconstructed image using the proposed method. (b) Line profiles of high-energy ground truth image and reconstructed image using the proposed method.

processing leads to images with substantial artifacts related to the streaky sinograms. In addition, without l_0 gradient minimization based smoothing, there are residual image artifacts and noise. After l_0 gradient minimization, the remaining artifacts are successfully removed. Table III summarizes the SSIM results for the cases of (b), (c), and (d) in Figs. 8 and 9. As shown in Figs. 8 and 9 and also in Table III, one can obtain anatomical structural information comparable to the gold standard image by the proposed method although the CT number in each pixel may not agree each other. We would like to note that, in the conventional MVUS methodology which directly uses the compressed-sensing inspired reconstruction algorithm for image reconstruction from sparsely sampled data, anatomical details can possibly be lost or smoothed in part. Instead, the proposed method provides an intact anatomical structure information as a prior that can help preserve important diagnostic image information in the dual-energy image reconstruction.

Figures 10 shows (a) low-energy ground-truth image, (b) high-energy ground-truth image, (c) low-energy reconstructed image and (d) high-energy reconstructed image using the iterative image reconstruction as described in the method section. Figure 11 (a) and (b) show the corresponding line profiles of the low- and high- energy ground-truth images, respectively, along red lines shown in Fig. 10 (a). Note that the reconstructed pixel values using the proposed method are in a good agreement with the ground-truth.

Figures 12 and 13 show the material-specific images after material decomposition. In both figures, (a) shows the soft-tissue, (b) the bone, (c) the air, and (d) the combined image in a pseudo-coloring scheme. It is notable that not only soft- and hard-tissue images but also air fraction image are successfully represented. In the simulation study, we have shown that the proposed method can successfully reconstruct the dual-energy anatomical images and can decompose the CT image into tissue-dependent maps.

B. Experimental Results

Figure 14 shows the experimental results of the initial image reconstruction step. Reconstructed images are represented in an array of 512 by 512 pixels with the pixel size of about 700 μm. Top-row images present the reconstructed images of the homogeneous part of Catphan phantom, middle-row images show the reconstructed images of the contrast part of Catphan phantom, and bottom-row images present the reconstructed images of the head phantom. Left-column images show the reconstructed images from the streaky sinogram by use of FBP algorithm without any processing,

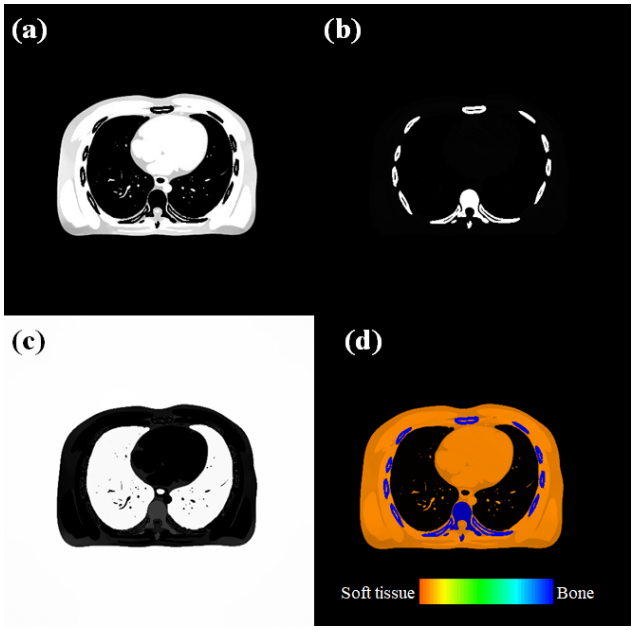

Fig. 12. Material decomposed images of (a) soft tissue, (b) bone, and (c) air, and (d) the combined image with pseudo-coloring.

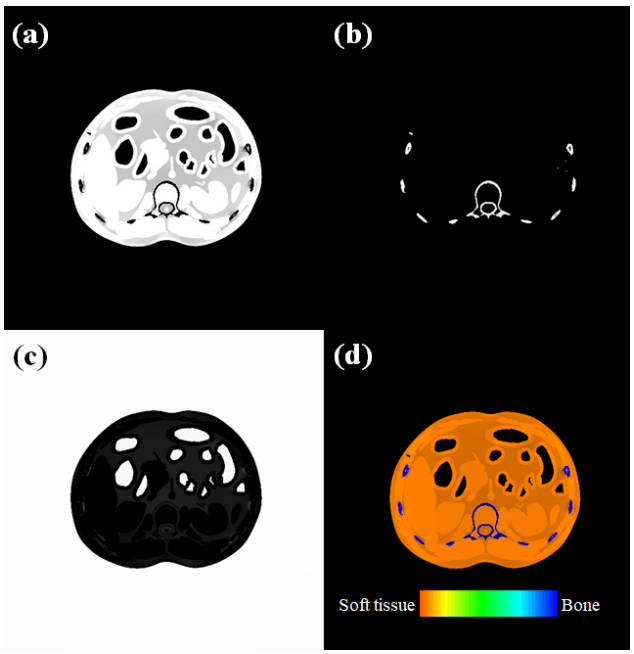

Fig. 13. Material decomposed images of (a) soft tissue, (b) bone, and (c) air, and (d) the combined image with pseudo-coloring.

and right-column images show the reconstructed images by use of the proposed method. It is visually obvious that the proposed method can lead to image reconstruction that is free of streaky sinogram related image artifacts. The image artifacts appear to be slightly different from those in the simulation study, which is due to their different object support sizes. The object support size with respect to the FOV in the experimental study was smaller than that of the simulation study, and the artifacts turn out to be less intruding the overall object image. In the image uniformity point of view,

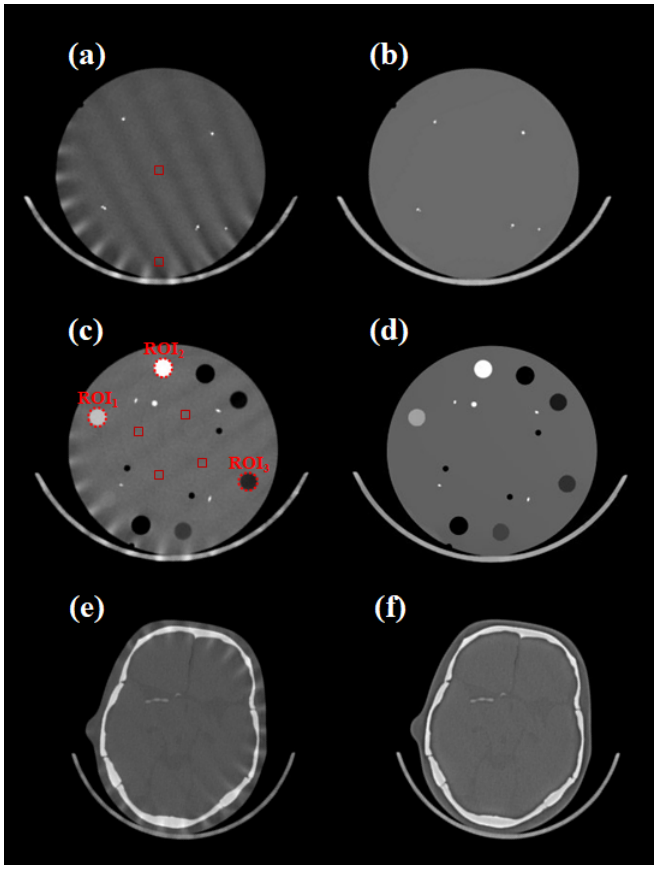

Fig. 14. (a), (c), (e) Reconstructed images using FBP without any processing. (b), (d), (f) Reconstructed images using the proposed method. The display window is [0.0088 mm^{-1}, 0.0337 mm^{-1}].

TABLE IV
COMPARISON OF CONTRAST VALUES BETWEEN (c) AND (d) IN FIG. 14 FOR VARIOUS REGIONS OF THE CONTRAST PART OF CATPHAN PHANTOM

Contrast	ROI_1	ROI_2	ROI_3
(c)	0.382	0.882	0.018
(d)	0.417	0.939	0.070

Figs. 14 (a) and (b) were used for evaluation. We calculated t_{cup} by using the red box ROIs. Value of t_{cup} in Fig. 14 (a) has been reduced by 82.8% in Fig. 14 (b). Contrast and CNR were evaluated for ROIs of Delrin^{TM}(ROI_1), Teflon (ROI_2), and LDPE (ROI_3) with 4 red box backgrounds Fig. 14 (c) and (d), and the results are summarized in Table IV and V. The results convince that the proposed image processing for prior image reconstruction is successful. The proposed method also consistently produced an artifact-free image of the head phantom as shown in Fig. 14. (f).

Figure 15 shows the material-decomposed images of the contrast part of the Catphan phantom. We assume that PMP represents soft-tissue and Teflon represents bone. Figure 15 (a) presents the reconstructed PMP-based image, (b) shows the reconstructed Teflon-based image, (c) shows the air fraction

TABLE V
COMPARISON OF CNR VALUES BETWEEN (c) AND (d) IN FIG. 14 FOR VARIOUS REGIONS OF THE CONTRAST PART OF CATPHAN PHANTOM

CNR	ROI_1	ROI_2	ROI_3
(c)	1.14	2.53	0.053
(d)	23.1	58.8	4.97

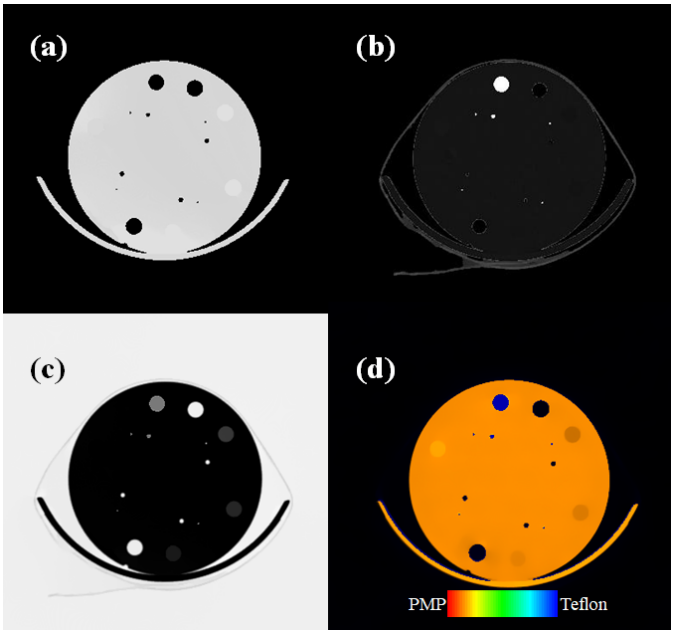

Fig. 15. (a) PMP-based image, (b) Teflon-based image, (c) air-fraction image, and (d) the combined image with pseudo-coloring of the Catphan phantom.

image, and (d) shows the combined image in a pseudo-coloring scheme. Similarly, Figs. 16 and 17 show the corresponding results of the head phantom and cardiac slice of a monkey scan, respectively. The experimental results consistently show that the proposed method can successfully reconstruct the image and decompose the image into material-specific maps.

Figure 18 shows the material-decomposed pseudo-colored images of the iodine-solution phantom using (a) a double scanning method as reference and (b) the proposed MVUS method. In Fig. 19, the calculated iodine concentrations from the images are plotted against true concentration values. Overall, they are all in a good agreement with the actual concentrations.

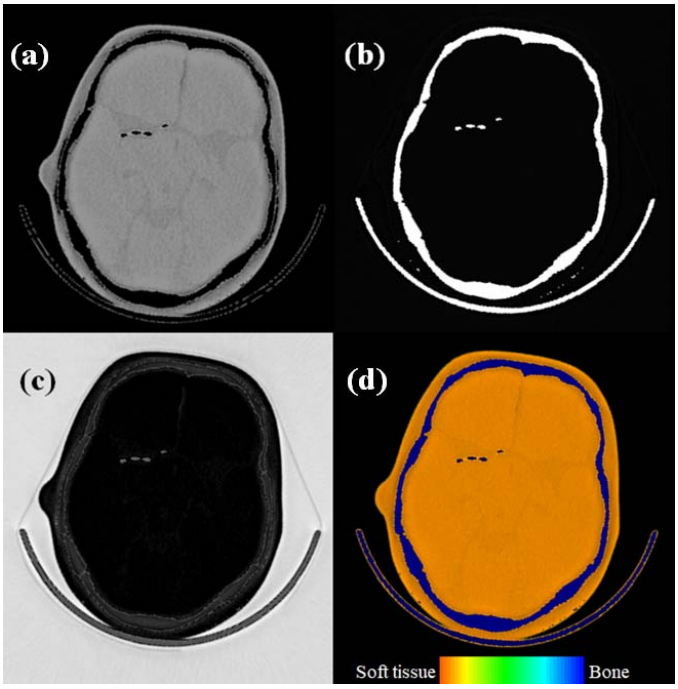

Fig. 16. (a) Soft tissue-based image, (b) bone-based image, (c) air-fraction image, and (d) the combined image with pseudo-coloring of the head phantom.

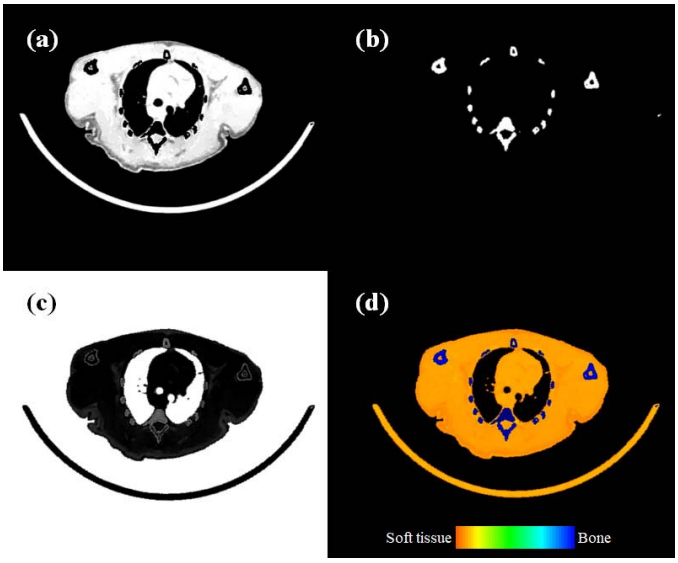

Fig. 17. (a) Soft tissue-based image, (b) bone-based image, (c) air-fraction image, and (d) the combined image with pseudo-coloring of the monkey cardiac.

IV. DISCUSSIONS

Through the simulation and experimental studies, we have shown that the proposed slanted multi-slit beam-filter based MVUS scanning and its associated image reconstruction method work successfully in a diagnostic CT system. Although actual dose reduction has not been quantitatively assessed in this work, it is with no doubt that the beam-filtration for high-energy projection data acquisition within a single projection FOV would reduce the overall patient dose compared to conventional dual-energy CT scan. Therefore, a single-scan low-dose dual-energy capability can be realized with a relatively simple hardware addition in a fast-rotating gantry-type CT imaging system. We would like to note that the conventional tube voltages and currents are widely varying depending on the scanning targets and protocols. For example, the tube current reported in the literature finds its value from 100 mA to 250 mA in conventional scanning protocols. We therefore believe the choice of our experimental conditions is not particularly biased toward extra-low noise data acquisition.

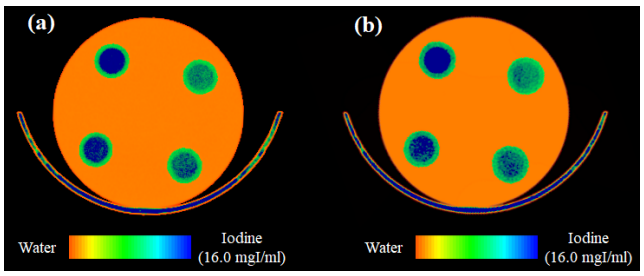

Fig. 18. (a) Double scanning based dual-energy image, and (b) proposed MVUS based dual-energy image with pseudo-coloring of the iodine phantom.

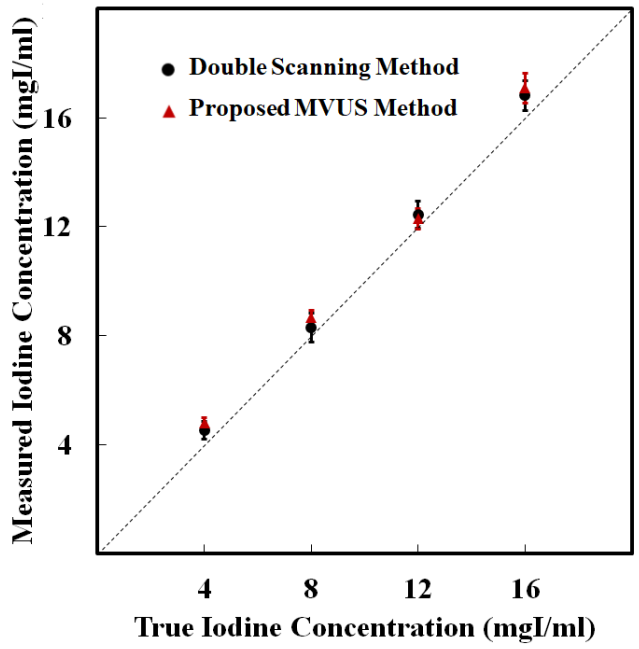

Fig. 19. Measured iodine concentrations using double scanning based method (reference) and proposed method. All error bars indicate standard deviation from the mean.

Indeed, the dose reduction in the proposed method primarily comes from the beam-filtration of about half of the lateral field-of-view in total, which would contribute to lowering the patient dose more than 40% compared to a conventional single energy scan. Moreover, it is the strength of the proposed method that the dual-energy data can be harvested at such a reduced dose condition. Full assessment of the imaging dose versus image quality in the proposed methodology within the clinical context will be conducted in our future study.

By the way, beam-filter based single-scan dual-energy imaging has recently been adopted in a commercialized clinical CT scanner (Siemens, Twin-beam CT) [51], [52]. The x-ray beam is split into two portions along the rotation axis direction and the low- and high-energy projections are acquired in a slice-by-slice manner. It is not straightforward to make an apples-to-apples comparison of this approach with the proposed one, but we would like to emphasize that the proposed method actively exploits sparse sampling scheme while the other one does not seem to do so.

Unlike our earlier demonstration of single-scan low-dose dual-energy imaging on the CBCT setting, the proposed method uses a linear motion of the beam-filter at a much slower motion speed. Because of the constant linear motion, there is nearly no acceleration of the beam-filter during a scan and it allows a stable and robust use of the motorized system. More importantly, reciprocating beam-filter would lead to a sinusoidal pattern of multi-slits in the sinogram. Removing such a pattern would be much more challenging, if not impossible, than the one presented in this work by use of the linear motion of the slanted multi-slit beam-filter.

In the initial image reconstruction, we have used the FBP algorithm from the streak-removed data. It is positive that the most widely used analytic algorithm is employed in this work since the reconstructed images by such analytic algorithms are familiar to the radiologists in general. The HU values of such prior image may represent the effective attenuation map at certain single x-ray energy between the low- and high-energy used in the scan. However, the accuracy of the HU values is not guaranteed and is thought to be hard to assess due to the nonlinear nature of the image processing steps involved in preparing the prior image in this work. Definitely, dual-energy imaging capability would add diagnostic values, but the radiologists or physicians may often need a conventional CT image as well in a short image reconstruction time. Although quantitatively not accurate, the initial reconstruction itself in this work can provide useful image information in such circumstances. Of course, the low-energy image reconstruction in the second step of the proposed reconstruction pipeline would yield a quantitatively more accurate image at an additional computational cost.

Only a circular fan-beam CT has been considered in this preliminary study. Helical fan-beam CT, however, is indeed the commonly used scanning configuration in practice. We believe it is straightforward to adapt the algorithm for such helical fan-beam CT scan. Using similar image processing techniques, one would be able to reduce streaks in the helical fan-beam sinogram. The helical fan-beam sinogram is typically interpolated to derive multiple circular fan-beam sinogram, and each slice image reconstruction is performed by using such interpolated circular fan-beam sinogram. Therefore, the proposed method should work in the helical scanning mode as well, and we are going to conduct the study in the future.

Further research would also include an improved beam-filter design and tailored parameter tunings for achieving optimum image quality. For example, a finer engineering of the curved beam-filter for reduction of penumbra would lead to a sharper discontinuity between the filtered and unfiltered regions in the sinogram. The sharper the discontinuity becomes, the easier the streak-removal becomes by use of the notch filter. In addition, in reconstructing low- and high-energy images, more data can be utilized while reducing the amount of discarded data. Also, along with the dose evaluation, efforts should be exerted on exploring optimum beam-filter thickness and area with respect to image quality.

V. Conclusion

In this preliminary study, we proposed a new scanning method that uses a sliding multi-slit beam-filter for dual-energy imaging in a fast-rotating gantry-type CT scanner.

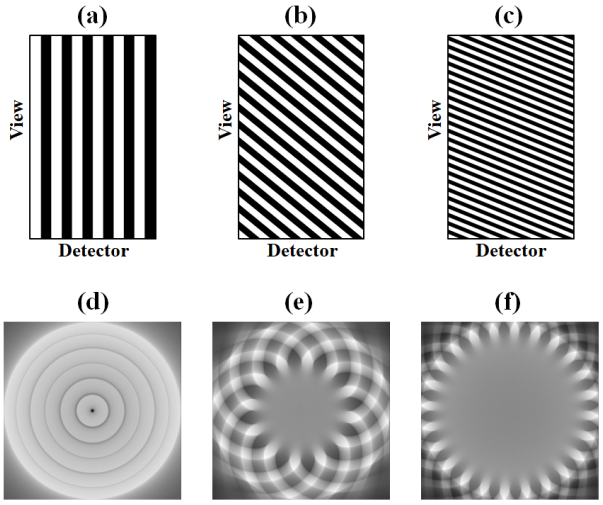

Fig. 20. Sinogram streak patterns corresponding to (a) 0-cycled (static beam-filter), (b) 2-cycled, and (c) 4-cycled streaks per gantry rotation. 2D SD distributions of (d) 0-cycled (static beam-filter), (e) 2-cycled, and (f) 4-cycled streaks per gantry rotation.

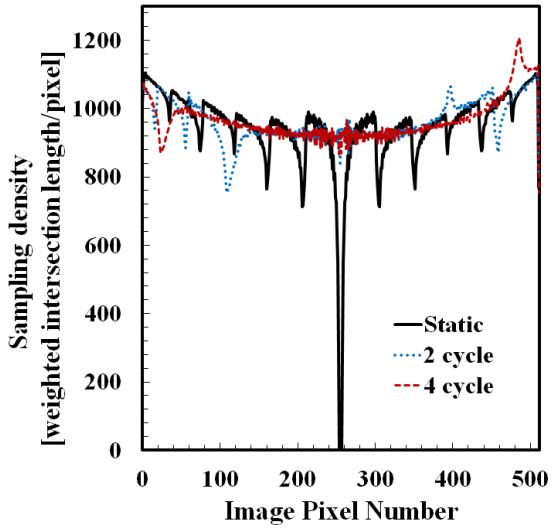

Fig. 21. Midline profiles of the SD maps of (d) 0-cycled (static beam-filter), (e) 2-cycled, and (f) 4-cycled streaks per gantry rotation.

We developed a notch-filter based streak removal process in the sinogram and l_0 gradient minimization of the image gradient for denoising in the image. Based on this prior image, we reconstructed dual-energy CT images and performed a material decomposition. Through simulation and experimental studies, we have successfully demonstrated the feasibility of the proposed method. We believe this technique would add substantially to the CT imaging field particularly in terms of enabling low-dose dual-energy imaging in the existing low-end CT systems.

Appendix

We show here the optimization process of the beam-filter design with the penumbra in consideration. As has been investigated in the earlier work in sparsely sampled CT imaging, sampling density (SD) is defined to yield the sum of intersections of the rays passing through a given pixel in the image domain as following [21]:

$$\mathrm{SD} = \sum_{m=1}^{M_n} d_{m_n} \tag{A1}$$

where d_{m_n} is the intersection length of the mth ray and the nth image pixel, and M_n is the total number of rays passing through the nth image pixel.

Figures 20 (a) - (c) show various sinogram streak patterns corresponding to 0-cycled (static beam-filter), 2-cycled, and 4-cycled streaks per gantry rotation, and Figs. 20 (d) - (f) show the corresponding SD maps. Figure 21 shows the horizontal midline profiles of the SD maps in Figs. 20 (d) - (f). As shown in the figures, SD becomes more uniform as the streak cycles increase. We would also like to emphasize that the moving beam-filter is more advantageous than the static one in the compressed-sensing inspired algorithm for sparsely sampled CT imaging.

With the use of slanted filter strips being justified, we have simulated SD at various cycles (1.5, 2, 2.5, 3, and 3.5 cycle)

TABLE VI
Simulated Ratio of Penumbra Region (%) With Respect to Number of Strips and Cycle

Cycle \ Strips	2	6	10	14
1.5	2.72	8.16	13.60	19.04
2	3.60	10.80	18.00	25.20
2.5	4.51	13.56	22.60	31.64
3	5.40	16.20	27.00	37.80
3.5	6.32	18.96	31.60	44.24

for varying number of strips (2, 6, 10, and 14 strips) considering the penumbra effects. Simulated ratios (%) of the penumbra over the entire FOV are listed in Table VI. The root-mean-square error (RMSE) from the ideal uniform case for each streak pattern was calculated and plotted in Fig. 22. Optimum parameters were found to be 6 strips and 3 cycles/rotation. Note our experimental conditions are near the optimum ones acquired in the numerical simulation.

For the filter material, Sn was used which was found to be an ideal material for its cost, machinability, and good energy separation performance [53]–[55]. Beam-filter thickness has a direct impact on the amount of mean energy shift and the surviving number of photons. 1 mm-thick Sn, similar to the ones typically reported in the related research articles, used in this study leads to about 3.3 % of surviving photons, 37 keV mean energy shift at the tube setting in this study, and 5.5 times higher projection noise level than the unfiltered projection, which are believed to yield near-optimum filter condition for the purpose of this feasibility study. Thinner filter may lead to an insufficient mean energy separation, and thicker filter may lead to increased amount of penumbra and much noise amplification. Sub-millimeter-scale thickness

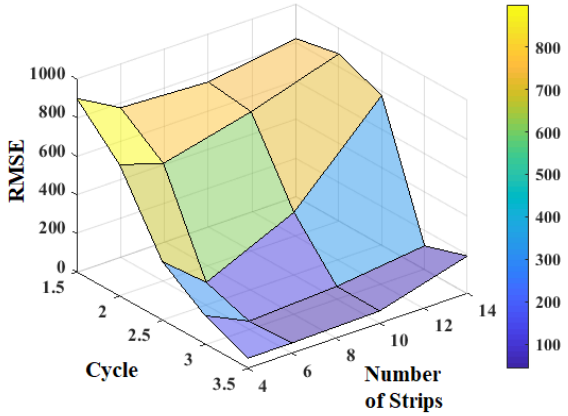

Fig. 22. RMSE from the ideal uniform case for each streak pattern.

refinement or optimization should be discussed in another work that focuses on dose versus image quality optimization in the clinical context.

REFERENCES

[1] S. Singh *et al.*, "Adaptive statistical iterative reconstruction technique for radiation dose reduction in chest CT: A pilot study," *Radiology*, vol. 259, no. 2, pp. 565–573, May 2011.

[2] K. Grant and R. Raupach, "SAFIRE: Sinogram affirmed iterative reconstruction," Siemens Med. Solutions, White Paper, 2012. [Online]. Available: http://usa.healthcare.siemens.com/siemens_hwem?hwem_ssxa_websites?context?root/wcm/idc/siemens_hwem?hwem_ssxa_websites?context?root/wcm/idc/groups/public/@us/@imaging/@ct/documents/download/mdaw/ndq2/~edisp/safire?00308312.pdf

[3] K. Sauer and C. Bouman, "A local update strategy for iterative reconstruction from projections," *IEEE Trans. Signal Process.*, vol. 41, no. 2, pp. 534–548, Feb. 1993.

[4] J. A. Fessler and A. O. Hero, "Penalized maximum-likelihood image reconstruction using space-alternating generalized EM algorithms," *IEEE Trans. Image Process.*, vol. 4, no. 10, pp. 1417–1429, Oct. 1995.

[5] C. A. Bouman and K. Sauer, "A unified approach to statistical tomography using coordinate descent optimization," *IEEE Trans. Image Process.*, vol. 5, no. 3, pp. 480–492, Mar. 1996.

[6] J.-B. Thibault, K. D. Sauer, C. A. Bouman, and J. Hsieh, "A three-dimensional statistical approach to improved image quality for multislice helical CT," *Med. Phys.*, vol. 34, no. 11, pp. 4526–4544, Oct. 2007.

[7] Z. Yu, J.-B. Thibault, C. A. Bouman, K. D. Sauer, and J. Hsieh, "Fast model-based X-Ray CT reconstruction using spatially nonhomogeneous ICD optimization," *IEEE Trans. Image Process.*, vol. 20, no. 1, pp. 161–175, Jan. 2011.

[8] T. Li *et al.*, "Nonlinear sinogram smoothing for low-dose X-Ray CT," *IEEE Trans. Nucl. Sci.*, vol. 51, no. 5, pp. 2505–2513, Oct. 2004.

[9] J. Wang, T. Li, H. Lu, and Z. Liang, "Penalized weighted least-squares approach to sinogram noise reduction and image reconstruction for low-dose X-Ray computed tomography," *IEEE Trans. Med. Imag.*, vol. 25, no. 10, pp. 1272–1283, Oct. 2006.

[10] P. J. La Rivière, "Penalized-likelihood sinogram smoothing for low-dose CT," *Med. Phys.*, vol. 32, no. 1, pp. 1676–1683, Jun. 2005.

[11] A. Manduca *et al.*, "Projection space denoising with bilateral filtering and CT noise modeling for dose reduction in CT," *Med. Phys.*, vol. 36, no. 11, pp. 4911–4919, Nov. 2009.

[12] L. I. Rudin, S. Osher, and E. Fatemi, "Nonlinear total variation based noise removal algorithms," *Phys. D, Nonlinear Phenomena*, vol. 60, nos. 1–4, pp. 259–268, Nov. 1992.

[13] S. Osher, A. Sole, and L. Vese, "Image decomposition and restoration using total variation minimization and the h-1 norm," *Multiscale Model. Simul.*, vol. 1, no. 3, pp. 349–370, Jul. 2003.

[14] Y.-L. Liu, J. Wang, X. Chen, Y.-W. Guo, and Q.-S. Peng, "A robust and fast non-local means algorithm for image denoising," *J. Comput. Sci. Technol.*, vol. 23, no. 2, pp. 270–279, Mar. 2008.

[15] D. J. Blezek, Z. Li, B. J. Bartholmai, A. Manduca, and B. J. Erickson, "Clinically feasible CT denoising using a GPU-based non-local means algorithm," in *Proc. Annu. Meeting Soc. Imag. Inform. Med.*, Washington, DC, USA, 2011.

[16] Z. Li *et al.*, "Adaptive nonlocal means filtering based on local noise level for CT denoising," *Med. Phys.*, vol. 41, no. 1, Jan. 2014, Art. no. 011908.

[17] M. Aharon, M. Elad, and A. Bruckstein, "K-SVD: An algorithm for designing overcomplete dictionaries for sparse representation," *IEEE Trans. Signal Process.*, vol. 54, no. 11, pp. 4311–4322, Nov. 2006.

[18] Q. Xu, H. Yu, X. Mou, L. Zhang, J. Hsieh, and G. Wang, "Low-dose X-Ray CT reconstruction via dictionary learning," *IEEE Trans. Med. Imag.*, vol. 31, no. 9, pp. 1682–1697, Sep. 2012.

[19] S. Li, H. Yin, and L. Fang, "Group-sparse representation with dictionary learning for medical image denoising and fusion," *IEEE Trans. Biomed. Eng.*, vol. 59, no. 12, pp. 3450–3459, Dec. 2012.

[20] M. Persson, D. Bone, and H. Elmqvist, "Total variation norm for three-dimensional iterative reconstruction in limited view angle tomography," *Phys. Med. Biol.*, vol. 46, no. 3, pp. 853–866, Mar. 2001.

[21] S. Abbas, T. Lee, S. Shin, R. Lee, and S. Cho, "Effects of sparse sampling schemes on image quality in low-dose CT," *Med. Phys.*, vol. 40, no. 11, Nov. 2013, Art. no. 111915.

[22] E. Y. Sidky and X. Pan, "Accurate image reconstruction in circular cone-beam computed tomography by total variation minimization: A preliminary investigation," *Phys. Med. Biol.*, vol. 53, pp. 4777–4807, Aug. 2008.

[23] J. S. Jorgensen, E. Y. Sidky, and X. Pan, "Quantifying admissible undersampling for sparsity-exploiting iterative image reconstruction in X-Ray CT," *IEEE Trans. Med. Imag.*, vol. 32, no. 2, pp. 460–473, Feb. 2013.

[24] J. Bian *et al.*, "Evaluation of sparse-view reconstruction from flat-panel-detector cone-beam CT," *Phys. Med. Biol.*, vol. 55, no. 22, pp. 6575–6599, Oct. 2010.

[25] J. Oh *et al.*, "Experimental study on the application of a compressed-sensing (CS) algorithm to dental cone-beam CT (CBCT) for accurate, low-dose image reconstruction," *J. Korean Phys. Soc.*, vol. 62, no. 5, pp. 834–838, Mar. 2013.

[26] S. Cho, "Feasibility study on many-view under-sampling technique for low-dose computed tomography," *Opt. Eng.*, vol. 51, no. 8, Aug. 2012, Art. no. 080501.

[27] T. Lee, C. Lee, J. Baek, and S. Cho, "Moving Beam-Blocker-Based low-dose cone-beam CT," *IEEE Trans. Nucl. Sci.*, vol. 63, no. 5, pp. 2540–2549, Oct. 2016.

[28] D. Lee *et al.*, "A feasibility study of low-dose single-scan dual-energy cone-beam CT in many-view under-sampling framework," *IEEE Trans. Med. Imag.*, vol. 36, no. 12, pp. 2578–2587, Dec. 2017.

[29] W. A. Kalender, W. H. Perman, J. R. Vetter, and E. Klotz, "Evaluation of a prototype dual-energy computed tomographic apparatus. I. phantom studies," *Med. Phys.*, vol. 13, no. 3, pp. 334–339, May 1986.

[30] Y. Zou and M. D. Silver, "Analysis of fast kV-switching in dual energy CT using a pre-reconstruction decomposition technique," *Proc. SPIE*, vol. 6913, Mar. 2008, Art. no. 691313.

[31] T. G. Flohr *et al.*, "First performance evaluation of a dual-source CT (DSCT) system," *Eur. Radiol.*, vol. 16, no. 2, pp. 256–268, Feb. 2006.

[32] L. Yu, A. N. Primak, X. Liu, and C. H. McCollough, "Image quality optimization and evaluation of linearly mixed images in dual-source, dual-energy CT," *Med. Phys.*, vol. 36, no. 3, pp. 1019–1024, Mar. 2009.

[33] R. Carmi, G. Naveh, and A. Altman, "Material separation with dual layer CT," in *Proc. IEEE Nucl. Sci. Symp. Conf. Rec.*, Oct. 2005, vol. 4, p. 3.

[34] K. Taguchi *et al.*, "Image domain material decomposition using photon counting CT," *Proc. SPIE*, vol. 6510, Dec. 2007, Art. no. 651008.

[35] X. Wang, D. Meier, K. Taguchi, D. J. Wagenaar, B. E. Patt, and E. C. Frey, "Material separation in x-Ray CT with energy resolved photon-counting detectors," *Med. Phys.*, vol. 38, no. 3, pp. 1534–1546, Mar. 2011.

[36] A. Sisniega *et al.*, "Volumetric CT with sparse detector arrays (and application to Si-strip photon counters)," *Phys. Med. Biol.*, vol. 61, no. 1, pp. 90–113, Nov. 2015.

[37] D. Zeng *et al.*, "Spectral CT image restoration via an average image-induced nonlocal means filter," *IEEE Trans. Biomed. Eng.*, vol. 63, no. 5, pp. 1044–1057, May 2016.

[38] M. Petrongolo and L. Zhu, "Single-scan dual-energy CT using primary modulation," *IEEE Trans. Med. Imag.*, vol. 37, no. 8, pp. 1799–1808, Aug. 2018.

[39] J. W. Stayman and S. Tilley, "Model-based multi-material decomposition using spatial-spectral lters," in *Proc. Int. Conf. Image Formation X-Ray Comput. Tomogr.*, 2018, pp. 102–105.

[40] M. Tivnan, S. Tilley, and J. W. Stayman, "Physical modeling and performance of spatial-spectral filters for CT material decomposition," *Proc. SPIE Med. Phys. Med. Imag.*, vol. 10948, 2019, Art. no. 109481A.
[41] P. Rattey and A. Lindgren, "Sampling the 2-D radon transform," *IEEE Trans. Acoust., Speech, Signal Process.*, vol. 29, no. 5, pp. 994–1002, Oct. 1981.
[42] S. R. Mazin and N. J. Pelc, "Fourier properties of the fan-beam sinogram," *Med. Phys.*, vol. 37, no. 4, pp. 1674–1680, Mar. 2010.
[43] L. Xu, C. Lu, Y. Xu, and J. Jia, "Image smoothing via L0 gradient minimization," *ACM TOG*, vol. 30, no. 6, Dec. 2011, Art. no. 174.
[44] D. Lee, H, Jo, and S. Cho, "Single-scan dual-energy CT image reconstruction via normalized gradient magnitude image (NGMI) regularization," in *Proc. 6nd Int. Meeting Image Formation X-Ray CT*, Regensburg, Germany, 2020, pp. 1–5.
[45] C. T. Badea, X. Guo, D. Clark, S. M. Johnston, C. D. Marshall, and C. A. Piantadosi, "Dual-energy micro-CT of the rodent lung," *Amer. J. Physiol.-Lung Cellular Mol. Physiol.*, vol. 302, no. 10, pp. L1088–L1097, May 2012.
[46] W. P. Segars, G. Sturgeon, S. Mendonca, J. Grimes, and B. M. W. Tsui, "4D XCAT phantom for multimodality imaging research," *Med. Phys.*, vol. 37, no. 9, pp. 4902–4915, Sep. 2010.
[47] A. A. Zamyatin, Y. Fan, K. Schultz, and S. Nakanishi, "Validation of compound Poisson noise model for computed tomography with energy-integrating detector," in *Proc. IEEE NSS/MIC*, Dec. 2012, pp. 2689–2691.
[48] T.-H. Kim *et al.*, "Development of mobile intraoperative computed tomography imaging system and assessment of its performance in a brain and body phantom study," *J. X-Ray Sci. Technol.*, vol. 27, no. 5, pp. 907–918, Oct. 2019.
[49] *Catphan 500 and 600 manual*, The Phantom Laboratory Salem, NY, USA, 2006.
[50] J. H. Siewerdsen, A. M. Waese, D. J. Moseley, S. Richard, and D. A. Jaffray, "Spektr: A computational tool for X-Ray spectral analysis and imaging system optimization," *Med. Phys.*, vol. 31, no. 11, pp. 3057–3067, Nov. 2004.
[51] I. P. Almeida *et al.*, "Dual-energy CT quantitative imaging: A comparison study between twin-beam and dual-source CT scanners," *Med. Phys.*, vol. 44, no. 1, pp. 171–179, Jan. 2017.
[52] R. K. Kaza and J. F. Platt, "Renal applications of dual-energy CT," *Abdom Radiol.*, vol. 41, pp. 1122–1132, Mar. 2016.
[53] A. N. Primak, J. C. Ramirez Giraldo, X. Liu, L. Yu, and C. H. McCollough, "Improved dual-energy material discrimination for dual-source CT by means of additional spectral filtration," *Med. Phys.*, vol. 36, no. 4, pp. 1359–1369, Apr. 2009.
[54] C. Thomas *et al.*, "Differentiation of urinary calculi with dual energy CT: Effect of spectral shaping by high energy tin filtration," *Investigative Radiol.*, vol. 45, no. 7, pp. 393–398, Jul. 2010.
[55] Y. Rakvongthai, W. Worstell, G. El Fakhri, J. Bian, A. Lorsakul, and J. Ouyang, "Spectral CT using multiple balanced K-Edge filters," *IEEE Trans. Med. Imag.*, vol. 34, no. 3, pp. 740–747, Mar. 2015.